Complex Pulse Profile Optimization by Chromatic Dispersion Management in Coupled Opto Electronic Oscillator based on Semiconductor Optical Amplifier

Alexis Bougaud, Arnaud Fernandez, Aliou Ly, Stéphane Balac, Olivier Llopis

Alexis Bougaud, Arnaud Fernandez, Aliou Ly, Stéphane Balac, Olivier Llopis. Complex Pulse Profile Optimization by Chromatic Dispersion Management in Coupled Opto Electronic Oscillator based on Semiconductor Optical Amplifier. IEEE Journal of Quantum Electronics, 2024, 60 (6), pp.1-9. 10.1109/JQE.2024.3372575 . hal-04790225

Complex Pulse Profile Optimization by Chromatic Dispersion Management in Coupled Opto-Electronic Oscillator based on Semiconductor Optical Amplifier

Alexis Bougaud, Arnaud Fernandez, Aliou Ly, Stéphane Balac and Olivier Llopis

***Abstract*—An Ikeda map iterative numerical model completed with an analytical Gaussian analysis and experimental measurements of complex pulse profile and phase noise performance at 10 GHz are proposed. This work aims to study and optimize the chromatic dispersion of a fibered mode-locked laser (MLL) based on a semiconductor optical amplifier (SOA) as part of a coupled optoelectronic oscillator (COEO). We will demonstrate that a close to zero anomalous dispersion regime is preferred as it allows the generation of optical picosecond pulses with minimum full width at half maximum (FWHM) and maximizes the absolute value of chirp and peak power. This guarantees the generation of narrow and diffraction-limited optical pulses after the chromatic dispersion compensating stage prior photodetection in order to lower the phase noise of the microwave signal generated at 10 GHz but also for high-order microwave harmonics synthesis.**

***Index Terms*—Optical pulses, semiconductor fiber ring laser, mode-locked lasers (MLLs), ultrafast optics, coupled optoelectronic oscillator (COEO).**

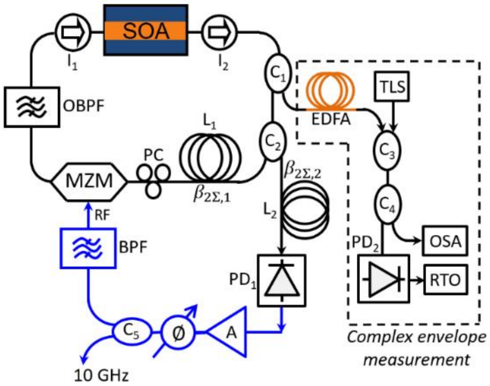

Fig. 1. Schematic of the COEO under experimental study accompanied by the stepped-heterodyne setup for pulse characterization. SOA: semiconductor optical amplifier, MZM: Mach Zehnder modulator, PC: polarization controller, OBPF: optical bandpass filter. I_1, I_2: optical isolators. $C_{1,2,3,4}$: optical couplers, L_1, L_2: optical fiber spools, PD_1, PD_2: photodiodes, A: RF amplifier, Ø: RF phase shifter, C_5: RF coupler, BPF: RF band-pass filter, EDFA: Erbium Doped Fiber Amplifier, TLS: tunable laser source, OSA: optical spectrum analyzer, RTO: real time oscilloscope.

I. INTRODUCTION

SINCE their apparition in the late 90's [1], COEO (Fig. 1) have demonstrated unprecedented results for highly spectrally pure microwave and millimeter-wave (mm-wave) signals synthesis using optical devices. Such device can generate a train of short optical pulses that are suitable for many applications, as to mention, RADAR and signal processing [2], [3].

A COEO generating a 10 GHz beat tone with -140 dBc/Hz phase noise at 10 kHz frequency offset was proposed by Matsko et al. [4], [5]. Based on a nearly similar design, Ly et al. have synthesized a 90 GHz frequency reference with lower than -120 dBc/Hz phase noise at 10 kHz frequency offset through third harmonic generation from a COEO operating at 30 GHz repetition rate [6].

Whether in fiber [4], [5], [6] or integrated technology [7], the conventional design of a COEO closely resembles that of a regenerative harmonically MLL laser (Fig. 1) but genuinely departs from it since the optical loop is stabilized so that the RF noise is minimized [3], [4]. The spectral noise purity of the RF drive determines the jitter of the optical pulses allowing a phase noise enhancement of the photo-generated RF signal compared to a classical harmonically MLL, limited by the external RF synthesizer phase noise performance. The dependence of the photodetected phase noise on pulses properties has been analyzed theoretically and experimentally [5], [8], [9].These studies demonstrate that a high energy and narrow pulse prior photodetection is of importance to reduce the timing jitter of mode-locked pulse train. Analytical [5] and semi-analytical studies [10], [11] have shown that group velocity dispersion (GVD) management in the optical cavity ($\beta_{2\Sigma,1}$, Fig. 1) can act favorably in the pulse peak power increase and its halfwidth decrease. For COEO employing a SOA [5], a $\beta_{2\Sigma,1}$ close to zero is optimal as it minimizes the optical pulse FWHM and

---

Manuscript submitted on September 20th, 2023. This work was supported by Region Occitanie and CNES (French Space Agency) under the SHYRO funding program.

A. Bougaud, A. Fernandez and O. Llopis are with the LAAS-CNRS, Université de Toulouse, CNRS, UPS, Toulouse, France, (corresponding author: phone: +33-561-7847; e-mail: afernand@laas.fr).

S. Balac is with the IRMAR, Université de Rennes 1, CNRS, Campus de Beaulieu, 35042 Rennes, France, e-mail : stephane.balac@univ-rennes1.fr).

A. Ly, is now with Laser Quantum Ltd, Stockport, UK.

maximizes its absolute value of chirp at the fiber spool input (L_2). Consequently, the external spool chromatic dispersion ($\beta_{2\Sigma,2}$ in Fig. 1) has to be adjusted in order to fully compensate this chirp. While these studies are relevant and highly useful, they lack precision and detailed interpretation concerning the behavior of COEO in the vicinity of null GVD. The study of COEO based on SOA considers the gain medium as a nonlinear component that instantly saturates compared to the pulse duration [5]. We will show that spectral and temporal distortion brought by SOA gain saturation, which is likely to be observed with pulses showing 10 ps FWHM and gain recovery time of 200 ps [12] has a strong impact on MLL steady state properties in the zero-dispersion area. Hence, we have developed a comprehensive and accurate numerical iterative model. The nonlinear chirp induced by gain saturation in the SOA is computed through a time domain evolution method. GVD and Kerr nonlinearity in optical fiber are described by the nonlinear Schrödinger equation, which is computed through the Runge Kutta 4 Interaction Picture algorithm that shows advantages in terms of ease of implementation and computational cost together with adaptive step-size control. A close look to the steady state property of the temporal and spectral complex envelope at the vicinity of each component in the optical loop is discussed in order to describe the physical effects leading to equilibrium. An analytical study based on a Gaussian approach will complete the discussions on the pulse properties and stability of the MLL close to a null GVD. Experimental measurements of phase noise performance and of the complex envelope through stepped-heterodyne method will corroborate our numerical and analytical analysis.

This paper is organized as follows. Section 2 brings a short description of COEO followed by a presentation of the numerical model. In section 3, our simulation results are interpreted and completed by an analytical Gaussian approach. Section 4 is mainly dedicated to experimental results referring to previous sections.

II. NUMERICAL MODEL

A. COEO principle

The architecture of our COEO, depicted in Fig. 1, was presented for the first time in 1996 by Yao et al. [1]. It is made of two coupled loops: an optical loop (black) and an opto-microwave loop (black and blue). The optical loop is a fiber ring MLL whose main components are a SOA acting both as an active medium and a source of light, and a MZM acting as a temporal gate. As both loops are sharing a common optical link, the COEO oscillation starts when Vernier effect between each cavity produces in-phase RF beat tone whose frequency is filtered by a dielectric bandpass filter centered at 10 GHz with 3 MHz bandwidth. Also, one must guarantee a sufficient gain so that oscillation build-up occurs. The solution to lower the phase noise of the microwave signal consists in building sufficiently long cavities in order to increase their Q factor thus enhancing the filtering effect of the phase noise. Coupled to a GVD management of the mode-locked loop leading to a close to zero total intracavity dispersion, we synthesized a 10 GHz signal with a phase noise of -120 dBc/Hz at 1 kHz frequency offset [13].

B. Ikeda map for COEO optical loop modeling

In order to simulate the optical cavity operation of our COEO, several simplifying approximations must be made. We have employed a numerical model for light wave propagation in the SOA and in the optical fiber spool. The effects of MZM and frequency bandpass filtering are taken into account through transfer functions. The physical parameters taken by the modeled components are reported in Table 1.

TABLE I
PHYSICAL PARAMETERS USED FOR NUMERICAL AND ANALYTICAL SIMULATION

	Symbol	Description	Value
Fiber	$L_{\Sigma,1}$	Length	472 m
	$\beta_{2\Sigma,1}$	Chromatic dispersion	-0.89 ps^2
	n_g	Group index	1.5
	$\gamma_{\Sigma,1}$	Nonlinear coefficient	0.72 W^{-1}
SOA	g_0	Small signal gain	39.3 cm^{-1} G_0=25.6 dB net gain
	α_{int}	Internal loss	3 cm^{-1}
	P_{sat}	Saturation power	14.9 dBm
	α_H	Henry factor	4
	τ_c	Carrier lifetime	200 ps
	L_{SOA}	SOA active length	1.5 mm
	$\Delta\omega_{SOA}$	Spectral broadening bandwidth	4.5 nm
MZM	K_0	Insertion loss	5 dB
	F_{rep}	RF frequency	10 GHz
	P_{RF}	RF power	20 dBm
	V_{DC}	DC polarization	3 V ($V_{\pi/2}$)
	δ_m	Modulation depth	0.57
Optical filter	H_0	Insertion loss	1 dB
	ν_0	Filtering frequency	193.4 THz
	$\Delta\nu_{-3\ dB}$	Bandwidth	20 nm
Optical loss	$\alpha_{\Sigma,TOT}$	Intracavity loss	2.8 (~12 dB)

Intracavity light propagation in optical fiber can be accurately described by the nonlinear Schrödinger equation (NLSE) for the slowly varying envelope $A(z,\tau)$ of the electric field where τ denotes the local time in a so-called moving frame travelling along with the optical envelope at group velocity $v_g = c/n_g$, with $\tau = t - z/v_g$. The linear and dispersive phenomena taken into account by NLSE are the linear attenuation through coefficient α and the dispersion through coefficients β_n (n = 2, 3, 4). Instantaneous nonlinear Kerr effect manifests itself through the term $j\gamma A(z,\tau)|A(z,\tau)|^2$.

$$\frac{\partial A(z,\tau)}{\partial z} = -\frac{\alpha}{2}A(z,\tau) - \sum_{n>1} j^{n+1}\frac{\beta_n}{n!}\frac{\partial^n A(z,\tau)}{\partial \tau^n} + j\gamma A(z,\tau)|A(z,\tau)|^2 \qquad (1)$$

When dealing with COEO devices where the optical pulse width is larger than 5 ps, excluding external cavity pulse compression, it is not necessary to include gain dispersion effect in SOA since its time constant is close to 0.1 ps [14]. Carrier recovery and gain saturation are the dominant effects in SOA (in this regime). Thus, light wave propagation in the SOA can be described by the following system of coupled equations

(2) and (3), where the unknown is A the slowly varying envelope propagating in the forward direction and g the gain rate. The parameters involved in equations (2) and (3) are described in Table (1).

$$\frac{\partial A(z,\tau)}{\partial z} = \frac{1}{2} g[(1 - j\alpha_H) - \alpha_{int}]A(z,\tau) \qquad (2)$$

$$\frac{\partial g(z,t)}{\partial t} = \frac{g_0 - g}{\tau_c} - g\frac{|A|^2}{E_{sat}} \qquad (3)$$

The MZM is biased at quadrature point and with an RF power (P_{RF}) at 10 GHz repetition frequency (F_{rep}) corresponding to RF amplifier saturation power located in the feedback loop. The transfer function is expressed as,

$$T_{MZM}(\tau) = \frac{K_0}{2}\left(1 + e^{j\pi\frac{V_{DC+v(\tau)}}{V_\pi}}\right) \qquad (4)$$

The bandpass filter is ideally represented as a high order Gaussian. We choose $m = 3$ to match with flat top filters.

$$\widetilde{H}_{BPF}(\nu) = H_0 e^{-\frac{1}{2}\left(\frac{\nu-\nu_0}{\Delta\nu}\right)^{2m}} \qquad (5)$$

To solve equations (1)-(5), we use a numerical scheme referred to as Ikeda map [15]. Starting with a low average power seeder (-40 dBm), modeled as a white Gaussian noise, it consists in computing separately and sequentially the slowly varying envelope $A(z,\tau)$ of the electrical field within the laser cavity components (optical fiber, SOA, MZM and bandpass filter) until a steady state pulse train is reached. The NLSE (1) can be solved very efficiently by the Interaction Picture (IP) method that can be seen as an improved symmetric split-step method combined with an embedded Runge-Kutta (RK) scheme with order 4 to solve the nonlinear part of the NLSE. It provides a robust and efficient step-size adaptive numerical method well suited for the purposes of the present study [16]. Equations (2) and (3) are two ordinary differential equations (with respect to the variable z for equation (2) and to the variable t for equation (3)). They are coupled through their right-hand sides that do not involve derivatives of the two unknowns A and g. These two equations are discretized using Euler method over a grid spanning the computational domain [0,L_{SOA}]x[0,t] for (z,t). A and g are computed at each grid node from their values at initial time t=0, taking into account boundary conditions at the fiber ends. This method is detailed in [17] in the context of bi-directional signal propagation. Ikeda map iterations end when a steady state regime is obtained.

III. NUMERICAL RESULTS AND DISCUSSIONS

A. Anomalous dispersion

The results displayed in Fig. 2 show the steady state pulse profile both in the temporal and in the spectral domain at different locations of the optical loop for a total chromatic dispersion $\beta_{2\Sigma,1}$ of $-0.89\ \mathrm{ps}^2$. This produces at coupler exit (C$_2$) a distorted pulse with an energy of 3.7 pJ, a peak power of 281 mW and a FWHM of 11.7 ps. Its instantaneous frequency denoted, $f_i(\tau) = -\frac{1}{2\pi}\frac{d\phi(\tau)}{d\tau}$, is monotonously decreasing and showing a quasi-linear negative slope (chirp) favored by anomalous dispersion such that $df_i/d\tau = -31\ \mathrm{GHz/ps}$.

The saturation of $h(\tau)$ is responsible for additive nonlinear chirp due to the self-phase modulation (SPM) induced by gain saturation expressed by: $\phi_{L_{SOA}}(\tau) = \phi_0(\tau) - \frac{1}{2}\alpha_H h(\tau)$ [12]. This nonlinear phase variation induces a distorted V shape instant frequency variation (Fig. 3), source of spectral red-shift and interference pattern in the power spectrum density (PSD) (Fig. 2b).

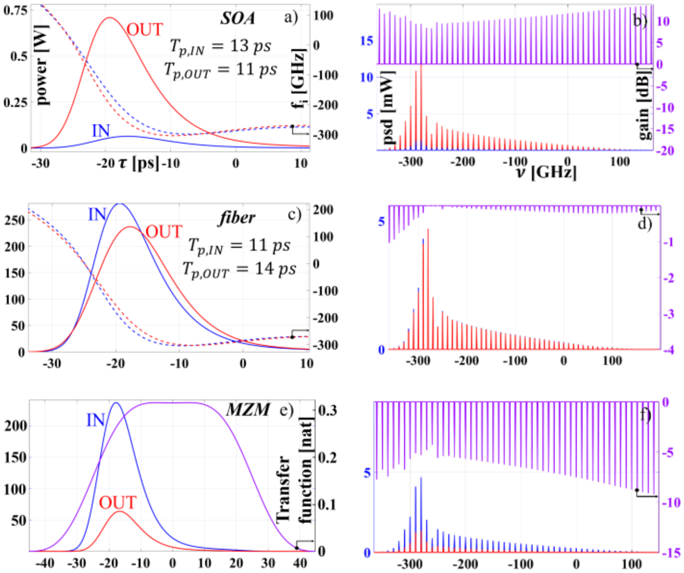

Fig. 2. Intra-cavity optical signal's progression under anomalous chromatic dispersion ($\beta_{2\Sigma,1} = -0.89\ \mathrm{ps}^2$): the input (blue) and output (red) signals in the temporal domain (left column) and spectral domain (right column) are juxtaposed. Each line is dedicated to a specific optical component (a-b: SOA, c-d: fiber spool, e-f: MZM). In the spectral domain, the violet curves represent the gain ratio (PSD$_{OUT}$/PSD$_{IN}$) expressed in dB, while in the temporal domain (e) the MZM gating effect is represented. Instantaneous frequencies are depicted in the temporal domain by dotted curves, with their color corresponding to the optical pulse shape.

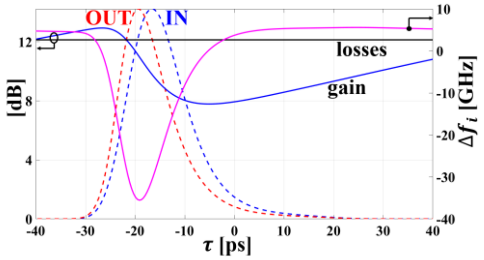

Fig. 3. In complement to Figure 2, this figure presents the normalized steady-state pulse profile upon entering (IN, dashed blue) and exiting (OUT, dashed red) the SOA. Additionally, it illustrates the associated integral gain $h(\tau)$ (solid blue) and the nonlinear instantaneous frequency variation Δf_i (solid pink) induced by self-phase modulation within the SOA.

At steady state the impact of SOA nonlinearity on instant frequency at each round trip is in the same order of magnitude than dispersive effects brought by optical fiber (see Fig. 2a and c). To maintain a steady state the SOA provides a sufficient 12 dB gain to balance the total cavity loss (Fig. 2a). Its nonlinear response distorts the temporal profile of the pulse (Fig. 3) by producing a steeper raising edge and a sharpened pulse profile. Higher gain $h(\tau)$ (see Fig. 3) at raising edge favors the amplification of high-frequency components (Fig. 2b) as the steady state shows a general negative chirp. The SPM effect induced by gain saturation at the vicinity of the amplified peak power tends to emphasize the negative instant frequency slope and red-shift. Propagation through the fiber spool L₁ is mainly ruled by group velocity dispersion effect that enlarges the pulse FWHM and compensate chirp increase in SOA (Fig. 2c). Finally, the MZM raising edge of the temporal gating effect will compensate the SOA temporal distortion effect thus producing a more symmetric pulse (Fig. 2e) and in the same time filtering high-frequency components (Fig. 2f).

B. Normal dispersion

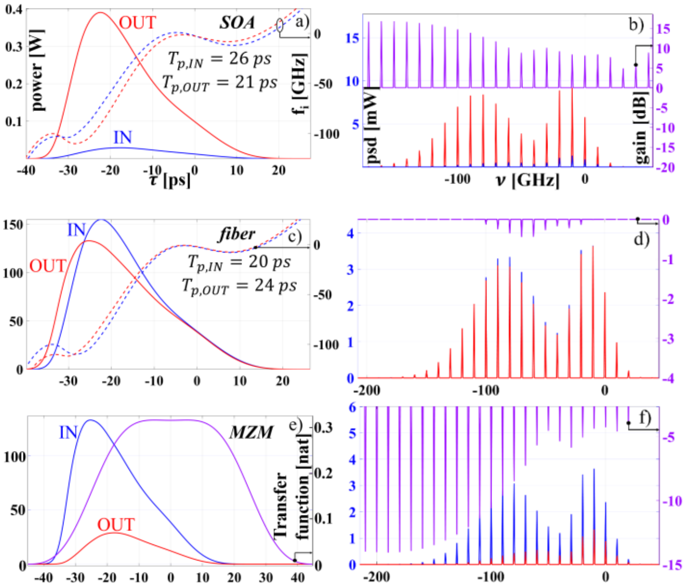

Fig. 4. Similar numerical results as in Fig. 3 but for a normal fiber dispersion $\beta_{2\Sigma,1} = 2.9$ ps^2.

In contrast to the anomalous dispersion case, the SOA nonlinear amplification favors the low frequency components (Fig. 4b). The carving of the instant frequency induced by SPM in SOA still creates red-shift but here increases the positive chirp across the pulse. Hence, we still observe similar values of instant frequency for two distinct points τ. This is responsible for interference pattern on the spectrum (Fig. 4b), which is characteristic of SPM in nonlinear media [12]. Similar to anomalous case, the chromatic dispersion effect from L₁ compensates the FWHM narrowing and chirp increase in SOA (Fig. 4c). Finally, the MZM raising edge of the temporal gating effect produces a more symmetric pulse (Fig. 4e) and filters the low-frequency components (Fig. 4f).

C. Pulse properties with chromatic dispersion

Changing properties of the steady state pulse as a function of $\beta_{2\Sigma,1}$ are discussed here. For comparison, we have observed and compared the steady state pulse peak power (P_{pk}), energy (ξ_p) (Fig. 5a), FWHM (τ_p), chirp (Fig. 5b), depending on $\beta_{2\Sigma,1}$ ranging between -8 and 12 ps^2 by adding to the 400 m initial length of SMF 28 (-22 ps^2.km^{-1}) an increasing length of DCF (115 ps^2.km^{-1}). The results were obtained by considering Kerr effect in the fiber spool. However, it is important to notice that similar results have been obtained without Kerr effect ($\gamma_{\Sigma,1} = 0$). Hence, in such fiber ring laser, the nonlinear Kerr effect in optical fiber plays a less important role due to moderate values of P_{pk}.

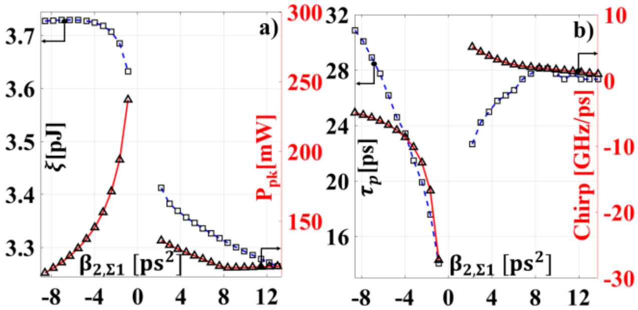

Fig. 5. Numerical results illustrating the variation of the steady state pulse parameters with $\beta_{2\Sigma,1}$. For all figures the blue dashed lines (square marks) and red plain lines (triangle marks) respectively refer to the left and right vertical axis.

The steady-state pulse profile is primarily shaped by the compensating interplay among SPM in SOA, GVD represented by $\beta_{2\Sigma,1}$ in optical fiber, and the gating effect of the MZM. The findings depicted in Fig. 5.a illustrate a decrease in pulse energy as $\beta_{2\Sigma,1}$ increases. This decrease is governed by the SOA saturation energy, influenced by electrical pumping, and the losses induced by the MZM, as demonstrated in Fig. 4e. However, τ_p, chirp and P_{pk} evolve monotonously as $|\beta_{2\Sigma,1}|$ decreases. Interestingly, as $|\beta_{2\Sigma,1}|$ approaches zero, we observe a steeper pulse narrowing and a simultaneous peak power and absolute value of chirp increase. Despite this behavior is not well detailed in the literature, this was already observed in previous semi-analytical studies on amplitude modulated (AM) [5], [11], [18] or frequency modulated (FM) [10] MLL. Moreover, we were unable to reach numerically a steady state regime for a total dispersion ranging between -0.45 and 2.5 ps^2. This reflects an instability of the MLL that manifest itself preferably in the normal dispersion regime.

A phenomenological explanation is however possible. Indeed, the SPM effect induced by the SOA will systematically add up in the same way to the positive chirp imposed by the dispersive fiber. For a normal dispersive case, the dynamic saturation of the SOA will exacerbate the red-shift effect by SPM and will shift the optical pulse toward the leading edge of the modulation window. As a result, the loss induced by the MZM will strongly affect the red components of the optical spectrum. The combined effect of the MZM and SOA leads to significant PSD variations per round trip thus destabilizing the MLL. For anomalous dispersion, the red-shift effect is partially compensated by the negative chirp, this explains why the MLL keeps its stability close to zero dispersion and thus allows narrower pulses with higher absolute value of chirp.

We will demonstrate analytically in the next section the evolution of chirp and pulse FWHM with $\beta_{2\Sigma,1}$. The existence of asymmetrical results of the pulse properties with dispersion regime and instability close to a zero chromatic dispersion will also be discussed.

D. Analytical approach

The numerical results presented in the previous part highlighted an instability area around zero dispersion which predominates in the normal dispersion regime (Fig. 5). This singularity has been rarely reported in literature, but is of prior importance in this paper dedicated to the dispersion management of COEO or even fibered MLL.

By using an analytical approach borrowed to Kuizenga et al. [19] we demonstrate that the instability is closely related to the nonlinear properties of the SOA, whose fast gain saturation and recovery produce new frequencies resulting in a systematic spectral enlargement that is proportional to the steady state pulse energy (Fig. 2b and Fig. 4b). Despite the spectral red-shift and distorted pulse profile observed numerically, and confirmed experimentally in the next section, we make the approximation of a complex Gaussian solution whose properties remain unchanged after one cavity round trip. This approximation facilitates the calculations both in the temporal and spectral domain, and yields to analytical results on the pulse halfwidth and chirp dependence to $\beta_{2\Sigma,1}$.

The Gaussian pulse solution is described by a complex envelope $A(\tau) = A_0\, exp(-\Gamma\tau^2) exp(j\omega_0 t)$ with $\Gamma = a - jb$. Also, the real part of Γ, $\mathcal{Re}(\Gamma) = 2ln2/\tau_p^2$, is inversely proportional to the quadratic FWHM, and its imaginary part is proportional to the chirp, $\mathcal{Im}(\Gamma) = -\pi df_i/d\tau$.

The steady state condition is determined by a self-consistent Gaussian solution. By assuming a pulse FWHM shorter than the modulation period, the complex pulse will undergo the gating effect of the MZM (6), with δ_m the modulation depth and $F_{rep} = \omega_m/2\pi$. The temporal operator describing the MZM is,

$$T_{MZM}(\tau) = exp(-\delta_m \omega_m^2 \tau^2) \tag{6}$$

Then the GVD induced by the optical fiber is preferably described in the spectral domain as follows,

$$\tilde{T}_{\beta_{2\Sigma,1}}(\omega) = exp(-j\beta_{2\Sigma,1}[\omega - \omega_0]^2/2) \tag{7}$$

The combined effect of spectrum enlargement and chromatic dispersion from the SOA is depicted as follows in the temporal domain,

$$T_{SOA}(\tau) = exp[(1 - j\alpha_H) g_2 \tau^2] \tag{8}$$

In equation (8), g_2 is related to the quadratic polynomial approximation of the pulse integral gain, $g(\tau)$, whose approximated solution applied to a Gaussian pulse train, issued from eq. (3), is given by eq. (9), with $\overline{g}$ the average saturated gain over the pulse train and ξ_p the pulse energy.

$$g(\tau) = \frac{g_0 - \overline{g}}{\tau_c}\tau - \frac{1}{2}\overline{g}\frac{\xi_p}{E_{sat}}\left(1 + erf\left(\frac{\tau}{\tau_p}\right)\right) \tag{9}$$

Hence, g_2 is expressed in eq. (10). As observed numerically in the anomalous (Fig. 2a) and normal (Fig. 4a) dispersive cases, the sign of g_2 refers to SOA nonlinear adaptation to the intra-cavity dispersive regime described by $\mathrm{sign}(\beta_{2\Sigma,1})$.

$$g_2 = sign(\beta_{2\Sigma,1})\frac{\overline{g}}{\tau_p^2\sqrt{2\pi}}\frac{\xi_p}{E_{sat}} exp\left(-\frac{1}{2}\right) \tag{10}$$

Hence, the SOA leads to the temporal Gaussian pulse shape variation $\Delta\Gamma_{SOA} = g_2(1 - j\alpha_H)$ which corresponds to the variation $\Delta(1/4\Gamma)_{SOA} = 4g_b/\Delta\omega^2 + j\beta_{2,SOA}/2$ of the Gaussian pulse Fourier transform. The real part of $\Delta(1/4\Gamma)_{SOA}$ expressed below, refers to a spectral broadening effect brought by the gain saturation and recovery in SOA. Moreover, its imaginary part refers to additive chromatic dispersion. Therefore, SOA and optical fiber contribute to an effective intra-cavity chromatic dispersion defined by:

$$\beta_2 = \beta_{2,SOA} + \beta_{2\Sigma,1} \tag{11}$$

By combining eq. (6), (7) and (8) we can express, after reasonable calculation step, a self-consistent Gaussian solution. The steady state pulse shape is expressed by the following expression.

$$\Gamma = \frac{\delta\omega_m^2}{2}\left(1 + \sqrt{1 + \frac{1}{\delta\omega_m^2\left(\frac{4g_b}{\Delta\omega^2} + j\frac{1}{2}\beta_2\right)}}\right) \tag{12}$$

with:

$$\frac{4g_b}{\Delta\omega^2} = -\frac{g_2[a^2 - b^2 + 2\alpha_H ab + g_2 a(1 + \alpha_H^2)]}{|2\Gamma(\Gamma + (1 - j\alpha_H)g_2)|^2} \tag{13}$$

and

$$\beta_{2,SOA} = \frac{g_2\left[\alpha_H\left(a^2 - b^2 - 2ab + g_2\left(a - b - \alpha_H(a + b)\right)\right)\right]}{2|\Gamma(\Gamma + (1 - j\alpha_H)g_2)|^2} \tag{14}$$

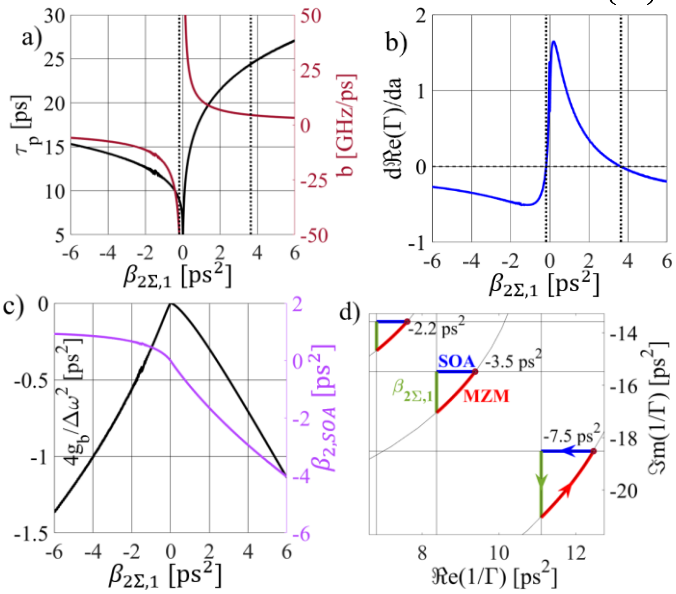

Fig. 6 .a) Pulse FWHM (τ_p) and chirp (b) solution of eq.(12) for an intra-cavity chromatic dispersion $\beta_{2\Sigma,1}$ ranging between -6 and 6 ps^2. The black vertical doted lines delimit the central instability area based on the criteria of stability given by eq.(16), obtained by the evaluation of $d\mathcal{Re}(\Gamma)/da$ illustrated in b) ; c) SOA spectral broadening (eq. 13) and chromatic dispersion contribution (eq. 14) depending on $\beta_{2\Sigma,1}$; d) Transformations $\tilde{T}_{MZM}$, $\tilde{T}_{SOA}$, $\tilde{T}_{\beta_2}$ occurring at steady-state in the $1/\Gamma$ plan for three distinct anomalous dispersive cases ($\beta_{2\Sigma,1}$) whose solution is presented in a). $\tilde{T}_{SOA}(\Gamma)$ has been separated here into its spectral broadening contribution $\tilde{T}_{4g_b/\Delta\omega^2}(\Gamma)$ (blue path) and its equivalent chromatic dispersion contribution ($\tilde{T}_{\beta_{2,SOA}}(\Gamma)$), so that the green path represents the effective chromatic dispersion in the MLL loop : $\tilde{T}_{\beta_2}(\Gamma) = \tilde{T}_{\beta_{2,SOA}}(\Gamma)$ $+ \tilde{T}_{\beta_{2\Sigma,1}}$.

Graphical interpretation of eq. (12) is given in Fig. 6. The respective pulse FWHM and chirp displayed in Fig. 6a, show a dependence to $\beta_{2\Sigma,1}$ that fairly correspond to the numerical results previously exposed in Fig. 5. It demonstrates that despite the SOA nonlinearity, source of pulse distortion, red-shift and nonlinear chirp through SPM effect (Fig. 2-4), it is yet possible to consider the interplay between the linear chirp induced by $\beta_{2\Sigma,1}$ and SOA with a Gaussian formalism. Thus, the linear chirp of the Gaussian pulse obtained with eq. (12) corresponds to the quasi-linear chirp, obtained from numerical results, located respectively at the pulse leading edge when $\beta_{2\Sigma,1} < 0$ and pulse trailing edge when $\beta_{2\Sigma,1} > 0$. It is also important to point out that the pulses asymmetry due to the SOA saturation, (Fig.3), infers higher energy located at the leading edge compared to the trailing edge of each individual pulses. The Gaussian approach proposed here is able to take into account this asymmetry by considering in eq. (9) two distinct pulse energy ξ_p depending on the sign of $\beta_{2\Sigma,1}$. It is by applying a ratio of 4 that we were able to obtain the asymmetrical results displayed in Fig. 6a.

This analytical description allows us to describe the mechanisms leading to the steady-state pulse increasing chirp and the pulse decreasing FWHM when $|\beta_{2\Sigma,1}|$ decreases. Indeed, this can be understood in the spectral domain in the $1/\Gamma$ plan (Fig. 6d). The SOA effect is represented by a complex contribution, $\tilde{T}_{SOA}$, showing an equivalent chromatic dispersion $\mathcal{Im}(\tilde{T}_{SOA}) = \beta_{2,SOA}$ (Fig. 6c (purple)) and a spectral broadening coefficient $\mathcal{Re}(\tilde{T}_{SOA}) = 4g_b/\Delta\omega^2$ (Fig. 6c (black)). We can then draw the effect of the effective chromatic dispersion β_2 (eq. (11)), represented by a vertical green path, while the SOA spectral broadening corresponds to a horizontal blue path. In a MLL configuration, the transformation imposed by the MZM is independent to $\beta_{2\Sigma,1}$ and follows a circular trajectory centered on its origin (red path, Fig. 6d). A steady state can then be reached whether Γ evolution at steady-state respect a close trajectory in the $1/\Gamma$ plan,

$$\tilde{T}_{MZM} + \tilde{T}_{\beta_{2\Sigma,1}} + \tilde{T}_{SOA}(\Gamma) = 0 \qquad (15)$$

thus, assuring the pulse shape recovery at each round trip. As $|\beta_{2\Sigma,1}|$ tends to 0, the length the fiber induced GVD path denoted $\left\|\overrightarrow{\tilde{T}_{\beta_{2\Sigma,1}}}\right\|$ gets shorter. Hence the steady-state solution Γ will be located at a position where $\left\|\overrightarrow{\tilde{T}_{SOA}}\right\|$ and $\left\|\overrightarrow{\tilde{T}_{MZM}}\right\|$ trajectories will also be decreased while conserving the closure condition, eq. (15). This will respectively reduce amplitude and phase modulation efficiency affecting both MZM and SOA transformations. As a consequence, we observe greater absolute chirp values and lower pulse FWHM as $|\beta_{2\Sigma,1}|$ tends to zero.

This graphical approach can then be completed by providing an analytical criterion on the MLL stability for a calculated steady-state value of Γ. A stable system needs to be robust to any pulse shape fluctuation. By assuming a Gaussian pulse of constant energy (ξ_p) for each chromatic dispersion regime, the SOA non-linearity only depends on τ_p (the pulse peak power being given by $P_{pk} = \xi_p/(\sqrt{\pi}\tau_p)$). Under such conditions, a stable oscillation is obtained whether:

$$\frac{d\mathcal{Re}(\Gamma)}{da} < 0 \qquad (16)$$

This stability criteria imposes that any pulse width fluctuation $\delta\tau_p$ must produce a variation of $\delta\mathcal{Re}(\Gamma)$ with the same sign. By looking at the sign of eq.(16), we are then able to delimitate the instability area as depicted by Fig. 6b. The broader instability area for $\beta_{2\Sigma,1} > 0$ results from a lower SOA non-linearity under normal chromatic dispersion leading to uneven path in the $1/\Gamma$ plan : $\left\|\overrightarrow{\tilde{T}_{SOA}}\right\|_{|\beta_{2\Sigma,1}|} < \left\|\overrightarrow{\tilde{T}_{SOA}}\right\|_{-|\beta_{2\Sigma,1}|}$.

Hence, those numerical and analytical approaches confirm that the interaction between a dispersive fiber and the SOA non-linearity favors the shortest pulses with highest absolute chirp value and peak-power by choosing a close to zero anomalous dispersion. This dispersive regime is of high interest for reducing the timing jitter of the optical pulse train by chirp compensation, and improving the RF phase noise of a COEO.

IV. EXPERIMENTAL RESULTS AND DISCUSSIONS

A. *Experimental setup*

The mode-locked optical cavity is designed as depicted in Fig. 1. The intracavity GVD of the optical cavity defined by $\beta_{2\Sigma,1}$ has been experimentally adjusted by using different spools of SMF (400 m, -23 ps^2.km^{-1}), DCF (55 m,115 ps^2.km^{-1}) and DSF (200 m,5 ps^2.km^{-1}) combined with two types of 4.2 nm bandwidth chirped fiber Bragg gratings (CFBG) centered at 1550.2 nm with respectively a group delay of ±9 ps^2 and ±33 ps^2. By combining the above listed dispersive components, we are able to provide an experimental study based on 15 different total intracavity chromatic dispersions ranging over a wide span between ∼-40 and 40 ps^2. The estimated total dispersion of the optical cavity based on the technical datasheet of the fiber and CFBG makes difficult to estimate $\beta_{2\Sigma,1}$ with a precision lower than 1 ps^2. It is crucial to highlight that for attaining low chromatic dispersion values, the (CFBG) was substituted with an unchirped tunable bandpass filter (TBPF) with the same bandwidth. The stability of oscillations is notably influenced at low intra-cavity chromatic dispersion. Therefore, fine-tuning the central wavelength of the TBPF enhances synchronization between MLL and the optoelectronic (OE) feedback loop, thereby improving overall oscillation stability.

A part from the intra-cavity chromatic dispersion management, the OE feedback loop include a 200 m spool of SMF, a 23.4 GHz bandpass PIN photodiode, a dielectric resonator centered at 10 GHz with 3 MHz bandwidth, a RF amplifier ($G_{RF} = 25$ dB, $P_{-1dB} = 21$ dBm) and a z-cut MZM polarized at quadrature. The synchronization between both loops is manually adjusted using a RF delay-line in the OE feedback loop and eventually the central wavelength of the OBPF whenever our TBPF is included in the MLL loop.

B. *Stepped-heterodyne measurements*

To validate the numerical results presented earlier, we utilized a well-established stepped-heterodyne technique [19], as illustrated in Fig. 1, to retrieve the complex pulse profile of the MLL. This technique captures the complex spectrum (amplitude and phase) of the MLL by mixing its signal with an optical local oscillator (TLS) placed between two signal modes. Recorded beat signals on a real-time oscilloscope (12.5 GHz bandwidth) and simultaneous acquisition of the MLL's PSD by an OSA enable the recovery of amplitude and phase differences between adjacent modes. By systematically stepping the local oscillator across all signal modes, we obtain a comprehensive measurement of the optical signal's amplitude and phase using

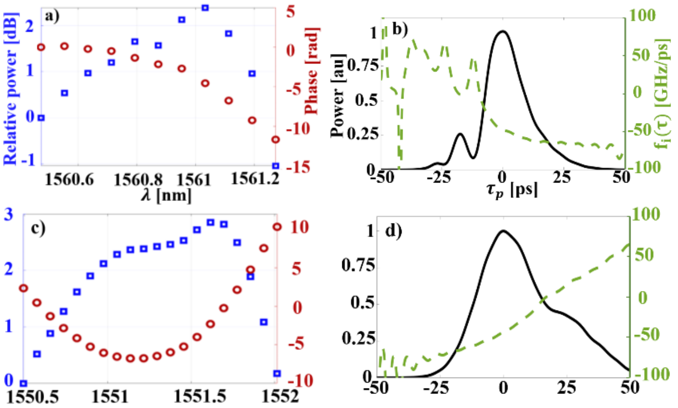

Fig. 7 Experimental results obtained using the stepped-heterodyne method in two cases of intracavity dispersion, $\beta_{2\Sigma,1}$, namely -2.86 ps^2 (a,b) and 7.9 ps^2 (c,d). For each dispersive case, figures a) and c) display the relative power spectrum density (blue square) and phase (red circles) of the spectral comb modes, the first measurable mode being taken as reference. Figures b) and d) display the deduced amplitude (plain black) and instant frequency (dashed green) of the complex pulse profile obtained by inverse Fourier transform of the corresponding measured complex spectrum (respectively a) and c)).

a recurrence method [19]. The temporal pulse profile is then derived through inverse Fourier transform.

Fig. 7 provides the experimental measured spectrum and the associated phase from which the temporal pulse profiles were recovered. A linear variation of the instant frequency corresponds to a quadratic phase profile that is both apparent on the complex temporal and spectral profile. The respective concavity or convexity of the quadratic phase refers to the steepness of the negative and positive instant frequency slope. The displayed measurements confirm that the instant frequency extracted from the recovered complex pulse evolves with a quasi-linear fashion in the vicinity of the pulse peak power.

In order to compare numerical and experimental results, we have run the stepped-heterodyne measurement with a large number of dispersive fibered samples in order to map the evolution of the pulse chirp and FWHM (Fig. 8a) with intracavity dispersion $\beta_{2\Sigma,1}$. Depending on the nature of the chromatic dispersion (anomalous or normal) and its magnitude, the sign and steepness of the instant frequency slope is affected as it was observed in the previous section. The pulse FWHM and chirp deduced from the stepped-heterodyne method are in good accordance with the numerical results displayed in Fig. 5b. In addition, measured spectral width depicted in Fig. 8b confirms the spectrum widening effect due to stronger chirp accumulation and pulse FWHM reduction as $|\beta_{2\Sigma,1}|$ decreases. Hence, optimal pulse compression by using the right amount of chromatic dispersion ($\beta_{2\Sigma,2}$) with fiber spool L_2 (see Fig. 1) is achievable by compensating the quasi-quadratic phase of the measured optical spectrum so that one obtains the flattest phase profile. The pulse compression was numerically estimated by compensating the quadratic part of the optical spectrum phase measured by stepped-heterodyne technique.

Application of this post-treatment to all the experimental values taken by $\beta_{2\Sigma,1}$ is depicted in Fig. 8a (red dots). With a GVD of -9 ps^2, we were then able to reduce the pulse FWHM from 31.4 ps to 12.5 ps which corresponds to a pulse width reduction of 60 %. Also, it is important to mention that the pulse compression ratio will be higher for an initially shorter pulse as their chirp increase with FWHM decrease [21]. As a consequence, the most favorable dispersion regime is obtained when $|\beta_{2\Sigma,1}|$ gets close to zero.

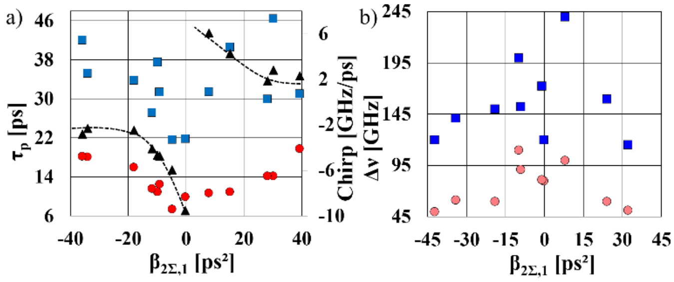

Fig. 8 a) Measurement with the stepped-heterodyne technique of the pulse FWHM (blue squares) and the instant frequency slope (black triangles) with the average optical cavity dispersion ($\beta_{2\Sigma,1}$). Calculated pulse FWHM at maximum of compression is given (red circle) through analytical chirp compensation applied to the experimentally measured pulses in order to simulate the impact of $\beta_{2\Sigma,2}$ in a COEO. b) Experimental measurement of the spectral width at -10 dB (red dots) and -50 dB (blue square) from the main mode.

Unfortunately, we were unable to adjust $\beta_{2\Sigma,1}$with a sufficient precision in order to appreciate the instability area and the pulse FWHM/chirp asymmetry numerically and analytically observed in the above section. For COEO optimization, a good approach to maximize the absolute value of the chirp in the low anomalous dispersion regime would consist in fine-tuning $\beta_{2\Sigma,1}$ without changing L_1 by using a mechanically tunable CFBG or programmable optical filters based on liquid crystal on silicon (LCoS) technology for instance.

C. *Phase noise*

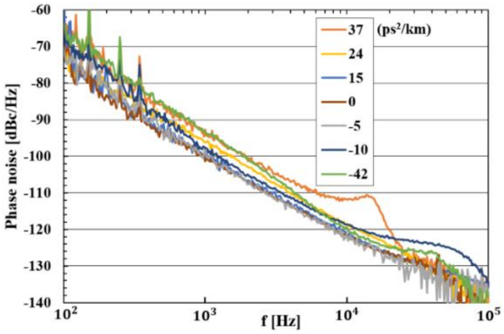

Fig. 9 Experimental phase noise measurement of the 10 GHz beat tone issued from the COEO for different $\beta_{2,\Sigma 1}$ (ps^2) values (see legend). These phase noise curves were selected to show the global impact of the chromatic dispersion on the RF phase noise. The passive quality factor of the optical loop is also corrected here to an equivalent 400 m fiber spool COEO.

Within the scope of COEO, it is essential to appreciate the effect of pulse compression on the phase noise of the 10 GHz RF beat note. The Fig. 9 shows the COEO phase noise dependence with a selected choice of experimental values of $\beta_{2\Sigma,1}$ and by keeping $\beta_{2,\Sigma 2}$ constant. The phase noise is lowered when $|\beta_{2\Sigma,1}|$ decreases. We can appreciate a phase noise reduction of 8 dB at 1 kHz offset from the 10 GHz carrier for a variation of 42 ps^2 of the intra-cavity GVD, as previously underlined theoretically [5]. However, by using different fiber spool length (L_1) in order to vary experimentally the intracavity dispersion, the passive quality factor of the optical loop is also modified. For this reason, the phase noise results presented here are plotted after correction of the passive quality factor for an equivalent 400 m fiber spool length COEO. Fig. 9 clearly shows the progressive phase noise reduction on the flicker part of the spectrum ($f < 5$ kHz) as $|\beta_{2,\Sigma 1}|$ gets close to zero. The small bump on phase noise curve around 50 kHz is due to the locking bandwidth between the optical and the optoelectronic feedback loop.

V. CONCLUSION

The paper introduces a numerical model, based on the Ikeda map, to predict and analyze mode-locked pulse behavior in a fibered AM MLL utilizing an SOA for COEO devices. The model reveals intricate interactions among the SOA's non-linearity, fiber GVD, and MZM gating effect, elucidating the establishment of a steady-state pulse profile. Emphasizing the significance of intra-cavity GVD effects near zero-dispersion, an analytical study employs a Gaussian pulse approximation to illustrate optical pulse properties and MLL stability. For an SOA-based MLL, stability in the laser favors minimal anomalous dispersion ($\beta_{2\Sigma,1}$), resulting in pulses with minimal FWHM, maximum chirp and peak power.

The model guides COEO device design, aiding in the accurate determination of $\beta_{2\Sigma,1}$ and the selection of optical components within the MLL loop for optimal compression before photodetection. This aligns with the reduction of oscillator phase noise, as previously predicted and experimentally demonstrated. Experimental validation using a stepped-heterodyne method confirms steady-state pulse properties and their dependence on intracavity dispersion, along with phase noise enhancement of the RF beat tone with decreasing dispersion.

The research lays the foundation for future COEO experimental endeavors, emphasizing the potential for precise tunability of $\beta_{2\Sigma,1}$ and $\beta_{2\Sigma,2}$ independent of optical cavity lengths, promising confirmation of theoretical insights, optimization of COEO phase noise, and the design of innovative COEO architectures.

ACKNOWLEDGMENT

The authors would like to acknowledge their partners B. Legrand (MEMS team), F. Caignet (ESE team) and PHOTO team members from LAAS-CNRS for fruitful discussions on the stepped-heterodyne method and for sharing the tunable laser sources and the 12 GHz real-time oscilloscope.

REFERENCES

[1] X. S. Yao and L. Maleki, “Optoelectronic microwave oscillator,” J. Opt. Soc. Am. B, JOSAB, vol. 13, no. 8, pp. 1725–1735, Aug. 1996, doi: 10.1364/JOSAB.13.001725.

[2] L. Maleki, “Optoelectronic oscillators for microwave and mm-wave generation,” in 2017 18th International Radar Symposium (IRS), Jun. 2017, pp. 1–5. doi: 10.23919/IRS.2017.8008133.

[3] F. Quinlan, S. Ozharar, S. Gee, and P. J. Delfyett, “Harmonically mode-locked semiconductor-based lasers as high repetition rate ultralow noise pulse train and optical frequency comb sources,” J. Opt. A: Pure Appl. Opt., vol. 11, no. 10, p. 103001, Aug. 2009, doi: 10.1088/1464-4258/11/10/103001.

[4] A. B. Matsko, D. Eliyahu, P. Koonath, D. Seidel, and L. Maleki, “Theory of coupled optoelectronic microwave oscillator I: expectation values,” J. Opt. Soc. Am. B, JOSAB, vol. 26, no. 5, pp. 1023–1031, May 2009, doi: 10.1364/JOSAB.26.001023.

[5] A. B. Matsko, D. Eliyahu, and L. Maleki, “Theory of coupled optoelectronic microwave oscillator II: phase noise,” J. Opt. Soc. Am. B, JOSAB, vol. 30, no. 12, pp. 3316–3323, Dec. 2013, doi: 10.1364/JOSAB.30.003316.

[6] A. Ly, V. Auroux, R. Khayatzadeh, N. Gutierrez, A. Fernandez, and O. Llopis, “Highly Spectrally Pure 90-GHz Signal Synthesis Using a Coupled Optoelectronic Oscillator,” IEEE Photonics Technology Letters, vol. 30, no. 14, pp. 1313–1316, Jul. 2018, doi: 10.1109/LPT.2018.2845747.

[7] L. Nielsen and M. J. R. Heck, “A Computationally Efficient Integrated Coupled Opto-Electronic Oscillator Model,” Journal of Lightwave Technology, vol. 38, no. 19, pp. 5430–5439, Oct. 2020, doi: 10.1109/JLT.2020.2981768.

[8] W. Zhang, T. Li, M. Lours, S. Seidelin, G. Santarelli, and Y. L. Coq, “Amplitude to phase conversion of InGaAs pin photo-diodes for femtosecond lasers microwave signal generation,” Appl. Phys. B, vol. 106, no. 2, pp. 301–308, 2012, doi: 10.1007/s00340-011-4710-1.

[9] F. Quinlan, T. M. Fortier, H. Jiang, and S. A. Diddams, “Analysis of shot noise in the detection of ultrashort optical pulse trains,” J. Opt. Soc. Am. B, JOSAB, vol. 30, no. 6, pp. 1775–1785, Jun. 2013, doi: 10.1364/JOSAB.30.001775.

[10] N. G. Usechak and G. P. Agrawal, “Rate-equation approach for frequency-modulation mode locking using the moment method,” J. Opt. Soc. Am. B, JOSAB, vol. 22, no. 12, pp. 2570–2580, Dec. 2005, doi: 10.1364/JOSAB.22.002570.

[11] N. G. Usechak and G. P. Agrawal, “Semi-analytic technique for analyzing mode-locked lasers,” Opt. Express, OE, vol. 13, no. 6, pp. 2075–2081, Mar. 2005, doi: 10.1364/OPEX.13.002075.

[12] G. P. Agrawal and N. A. Olsson, “Self-phase modulation and spectral broadening of optical pulses in semiconductor laser amplifiers,” IEEE Journal of Quantum Electronics, vol. 25, no. 11, pp. 2297–2306, Nov. 1989, doi: 10.1109/3.42059.

[13] R. Khayatzadeh, V. Auroux, A. Fernandez, and O. Llopis, “COEO phase locking and performance optimisation,” in 2017 Joint Conference of the European Frequency and Time Forum and IEEE International Frequency Control Symposium (EFTF/IFCS), Jul. 2017, pp. 489–492. doi: 10.1109/FCS.2017.8088936.

[14] G. P. Agrawal, “Effect of gain dispersion on ultrashort pulse amplification in semiconductor laser amplifiers,” IEEE J. Quantum Electron., vol. 27, no. 6, pp. 1843–1849, 1991, doi: 10.1109/3.90014.

[15] K. Ikeda, “Multiple-valued stationary state and its instability of the transmitted light by a ring cavity system,” Optics Communications, vol. 30, no. 2, pp. 257–261, Aug. 1979, doi: 10.1016/0030-4018(79)90090-7.

[16] S. Balac and A. Fernandez, “SPIP: A computer program implementing the Interaction Picture method for simulation of light-wave propagation in optical fibre,” Computer Physics Communications, vol. 199, pp. 139–152, Feb. 2016, doi: 10.1016/j.cpc.2015.10.012.

[17] J. W. D. Chi, A. Fernandez, and C. Lu, “Properties of Mode-Locked Optical Pulses in a Dispersion-Managed Fiber-Ring Laser Using Semiconductor Optical Amplifier as Active Device,” IEEE Journal of Quantum Electronics, vol. 49, no. 1, pp. 80–88, Jan. 2013, doi: 10.1109/JQE.2012.2230317.

[18] F. X. Kärtner, D. Kopf, and U. Keller, “Solitary-pulse stabilization and shortening in actively mode-locked lasers,” J. Opt. Soc. Am. B, vol. 12, no. 3, p. 486, Mar. 1995, doi: 10.1364/JOSAB.12.000486.

[19] D. Kuizenga and A. Siegman, “FM and AM mode locking of the homogeneous laser - Part I: Theory,” IEEE Journal of Quantum Electronics, vol. 6, no. 11, pp. 694–708, Nov. 1970, doi: 10.1109/JQE.1970.1076343.

[20] D. A. Reid, S. G. Murdoch, and L. P. Barry, “Stepped-heterodyne optical complex spectrum analyzer.,” Opt. Express, OE, vol. 18, no. 19, pp. 19724–19731, Sep. 2010, doi: 10.1364/OE.18.019724.

[21] Siegmann, Lasers, New édition. Mill Valley, Calif: University Science Books,U.S., 1986.

Alexis Bougaud received the Master’s degree from the department of Material Science Engineering of the National Institute of Applied Science of Rennes, France in 2017. Since 2018, he is working towards his Ph.D. degree in the field of phase noise optimization of coupled opto-electronic oscillators at LAAS-CNRS.

Arnaud Fernandez received the Master's degree in electronic engineering from the National Engineering School of Brest, Brest, France, in 2003, and the M.Sc. and Ph.D. degrees from the Université de Bretagne Occidentale, Brest, in 2004 and 2009, respectively. Since 2012 he is an Associate Professor at LAAS-CNRS. His current research interests include photonics, nonlinear optics, semiconductor device modeling, and optical communication technology. Dr. Fernandez is a member of the Société Française d'Optique.

Aliou Ly received the Master's degree in Sc. And Technologies from Institut d'Optique Graduate School, University of Paris Sud in 2014, and Ph.D. in physics from Aimé Cotton Laboratory, University of Paris Sud-11, Orsay. He joined in 2018 LAAS-CNRS, Toulouse, France, as a Post-Doctoral Researcher. Since 2019, he joined Laser Quantum Ltd, Stockport, UK.

Stéphane Balac is Assistant Professor at the Mathematics Research Institute of Rennes, University of Rennes. His research topics lie in the area of numerical analysis and mathematical modeling in physics.

Olivier Llopis received the diploma of Telecommunications engineer from ENSTB, Brest, in 1987 and the Ph.D. degree in Electronics from Université Paul Sabatier, Toulouse, in 1991. He is currently working with the French National Centre for Scientific Research (CNRS) in the Laboratoire d'Analyse et d'Architecture des Systèmes (LAAS) in Toulouse. At LAAS, he is involved in research projects in the microwave and optics department (HOPES) and he is also scientific delegate for space projects at the laboratory level. His personal research interests are in the study of microwave and optical sources, phase noise modeling and metrology.